

Log-likelihood-based rule for image quality monitoring in the MLEM-based image reconstruction for PET

Anastasios Gaitanis *Student Member, IEEE*, George Kontaxakis, *Senior Member, IEEE*, George Spyrou, George Panayiotakis, and George Tzanakos, *Senior Member, IEEE*

Abstract— We address here the problem of the noise deterioration of the quality of the reconstructed images when employing the maximum likelihood expectation maximization (MLEM) algorithm for iterative image reconstruction in positron emission tomography (PET). It is observed that despite the fact the cost function (log-likelihood) is monotonically increasing, the image quality deteriorates after reaching a certain “optimum” point during the iterative process. The principal aim of the work is the discovery of a rule that would directly link the quality of the reconstructed images at each iteration with the log-likelihood. We assume that the true image corresponds to a log-likelihood value in correlation with the data acquired, which, when achieved, makes no sense looking for higher log-likelihood levels. We study here the hypothesis that there is a direct correlation of the log-likelihood of the true image (a quantity that is not known a priori in real PET scans) and acquired data, with certain properties of the pixel updating coefficients (PUC) in the MLEM algorithm. For the validation of this hypothesis we have employed Monte Carlo experiments using known phantoms. We show here that the minimum value of the PUC for the non-zero pixels might be one parameter that could be used to verify the above mentioned hypothesis.

I. INTRODUCTION

Positron Emission Tomography (PET) can be used to give up images of the distribution of a radiopharmaceutical into the human body. PET is used in several clinical areas such as oncology, cardiology, neurology, etc. In modern PET scanners image reconstruction algorithms play an important role in the quality of the produced images. Nowadays the Maximum Likelihood Expectation Maximization (MLEM)

[1], Ordered Subsets Expectation Maximization (OSEM) [2] and their variants [3] are used.

It is well known that the MLEM algorithm produces images with better quality than other analytical techniques, however MLEM images are becoming noisier after a large number of iterations. At the same time, the objective function that is being maximized (log-likelihood) does monotonically increase and therefore the image with the highest log-likelihood value might not necessarily correspond to the best image. Previous works have suggested that maximizing the log-likelihood function might not be a good criterion to pursue, as the resulting image gets noisier [4]. To overcome this problem several methods have been investigated. One method is to stop the algorithm after an arbitrary number of iteration and then post-filter the reconstructed image [3]. Another method is to stop the iteration process based on a robust stopping rule. Several research groups in the past have proposed stopping rules for the MLEM algorithm [5]-[8] but these have not yet been employed in clinical setting.

Our group has proposed a methodology of an empirical stopping rule for the MLEM algorithm [7]-[9]. This work reports on the preliminary results of a novel approach to monitor the reconstructed image quality by correlating some specific properties of the pixel updating coefficients of the MLEM algorithm to the log-likelihood value that corresponds to the true activity distribution in the source and the data acquired.

II. MATERIALS AND METHODS

A. MLEM algorithm

In PET imaging the problem of image reconstruction is to estimate the true emission density \hat{x} from the acquired data vector y . The mathematical model that describes the MLEM-based image reconstruction process is based on the hypothesis that the emission in the source occurs according to Poisson statistics. The likelihood function $L(x)$ represents the probability under the Poisson probability model for emission to observe the measured counts if the true density was a given image vector x . In maximum-likelihood methodologies, typically the log-likelihood function (1) is taken and then maximized:

Manuscript received November 13, 2009.

A. Gaitanis is with the Department of Medical Physics, Medical School, University of Patras and Biomedical Research Foundation of Athens Academy, Soranou Efessiou 4, 11527 Greece (e-mail: agaitanis@bioacademy.gr).

G. Kontaxakis is with the Biomedical Image Technology Group, Universidad Politécnica de Madrid, and with the Biomedical Research Center of Bioengineering, Biomaterials and Nanomedicine (CIBER-BBN), 28040 Madrid, Spain (e-mail: g.kontaxakis@ieee.org).

G. Spyrou is with the Biomedical Research Foundation of Athens Academy, Soranou Efessiou 4, 11527 Greece (e-mail: gspyrou@bioacademy.gr).

G. Panayiotakis is with the Department of Medical Physics, Medical School, University of Patras, 26500 Patras, Greece (e-mail: panayiot@upatras.gr).

G. Tzanakos is with the University of Athens, Department of Physics, Division of Nuclear & Particle Physics, Panepistimioupoli, Zografou, Athens 15771, Greece (e-mail: tzanakos@phys.uoa.gr).

$$l(\mathbf{x}) = \log(L(\mathbf{x})) = \sum_{j=1}^J \sum_{i=1}^I x(i)^{(k)} \alpha(i, j) + \sum_{j=1}^J y(j) \log\left(\sum_{i=1}^I x(i)^{(k)} \alpha(i, j)\right) - \sum_{j=1}^J \log(y(j)!) \quad (1)$$

where i is the i th pixel in the image vector, \mathbf{x} is the image vector, $y(j)$ is the projected data in j th line-of-response (LOR) and $\alpha(i, j)$ represents the probability that an annihilation event generated in the area of the i th pixel is detected in the j th LOR; $\alpha(i, j)$ is also known as the system matrix for a given scanner configuration. The general form of MLEM algorithm that expresses the pixel updating process at the k iteration is:

$$x^{(k)}(i) = x^{(k-1)}(i) C^{(k-1)}(i) \quad (2)$$

$$C^{(k-1)}(i) = \frac{\sum_{j=1}^J \frac{y(j) \alpha(i, j)}{\sum_{i'=1}^I x^{(k-1)}(i') \alpha(i', j)}}{\sum_{i'=1}^I x^{(k-1)}(i') \alpha(i', j)} \quad (3)$$

where $C^{(k-1)}$ is the vector of the pixel updating coefficients (PUC) at the $(k-1)$ th iteration.

B. The PET scanner

We have modeled a single-ring PET camera with 128 scintillation crystals on the ring, a detector width of 7.36 mm and a field of view (FOV) of 200×200 mm². The detector ring radius is 150 mm. The total number of LOR is 8128. Image grids with a size of 128×128 (pixel side = 1.56 mm) have been employed. Custom Monte Carlo simulations (written in C) have been used for the simulation of the activity distribution in the source, the generation of positron-electron annihilations, the production of gamma-rays, their propagation in the source and their detection by the scintillation detectors. Ideal conditions have been assumed (100% detector efficiency, no Compton scattering or photoelectric effects in the source and the detectors, no random coincidences, etc.).

C. The system matrix

The system matrix depends on the geometry and configuration of the PET scanner (image grid and scanner's layout). Each matrix element $\alpha(i, j)$ represents the transition law from the image activity distribution $x(i)$ to the measured data $y(j)$. Hence the matrix element shows the geometrical acceptance of annihilation events generated in pixel i and detected by the LOR j . In this work, the transition matrix for the camera configuration employed has been calculated using Monte Carlo methods. In the area that corresponds to each pixel i a sufficient number of events N_{tot} were generated and the simulated gamma-rays were recorded in each LOR. The probability value $\alpha(i, j)$ is then given by the expression:

$$\alpha(i, j) = \frac{N_j}{N_{tot}} \quad (4)$$

where N_j is the number of those events detected within the j th LOR. The accuracy of this method depends on the total number of annihilation events generated in each pixel. For this reason 10^7 gamma-rays have been uniformly generated in each pixel. In that way the relative error is less than 1%.

D. Data generation

For this study the MOBY [10] and the digital Hoffman brain [11] phantoms have been used. The Hoffman brain phantom consists of 18 2-dimensional image slices and the MOBY phantom consists of 129 slices as shown in Fig. 1. The pixel values in each slice correspond to the activity distribution in the area covered by each pixel in the source. A proportional number of gamma rays have been generated using Monte Carlo methods for this pixel and their trajectories have been followed until they hit a detector on the camera's ring. For each slice various activity distributions have been simulated, ranging from 200,000 to 6.0 million counts. Using this procedure, data from the Hoffman brain and MOBY phantoms have been acquired at different activity distribution levels and have been reconstructed using the MLEM algorithm.

For the validation of the results obtained, we have used data acquired based on the Digimouse phantom [12] and according to a similar procedure as the one followed for the Hoffman and MOBY phantoms: based on the activity distribution in the Digimouse image slices, a predefined number of counts has been generated, assuming an ideal, noise-free case. These data have been then reconstructed using the MLEM algorithm.

E. Image quality monitoring

In the MLEM algorithm an initial estimate image $\mathbf{x}^{(0)}$ (typically a uniform activity distribution for all pixels) is used as starting point. The quality, as referred to the signal to noise characteristics, of the reconstructed image steadily improves during the first iterations however after a certain point the image quality starts getting significantly noisier. In order to monitor the noise levels in the reconstructed images, we calculate the log-likelihood value for the case of the simulations using the Hoffman and the MOBY phantoms according to (1), provided that in these cases both the phantom image and the detected counts per LOR are known. During the MLEM reconstruction, it is of no avail looking higher likelihood than the one inherent in the acquired data. Hence, when the log-likelihood at a certain iteration reaches the log-likelihood calculated based on the phantom measurements, there is no need to continue the iterative process:

$$\log(L(x))_{recon.image} \geq \log(L(x))_{phantom.image} \quad (5)$$

During a real PET scan, however, the quantity $\log(L(x))_{phantom.image}$ is not available. In the next section we describe a methodology that correlates the log-likelihood-related properties of the reconstructed image with the properties of the PUC, as given in eq. (3).

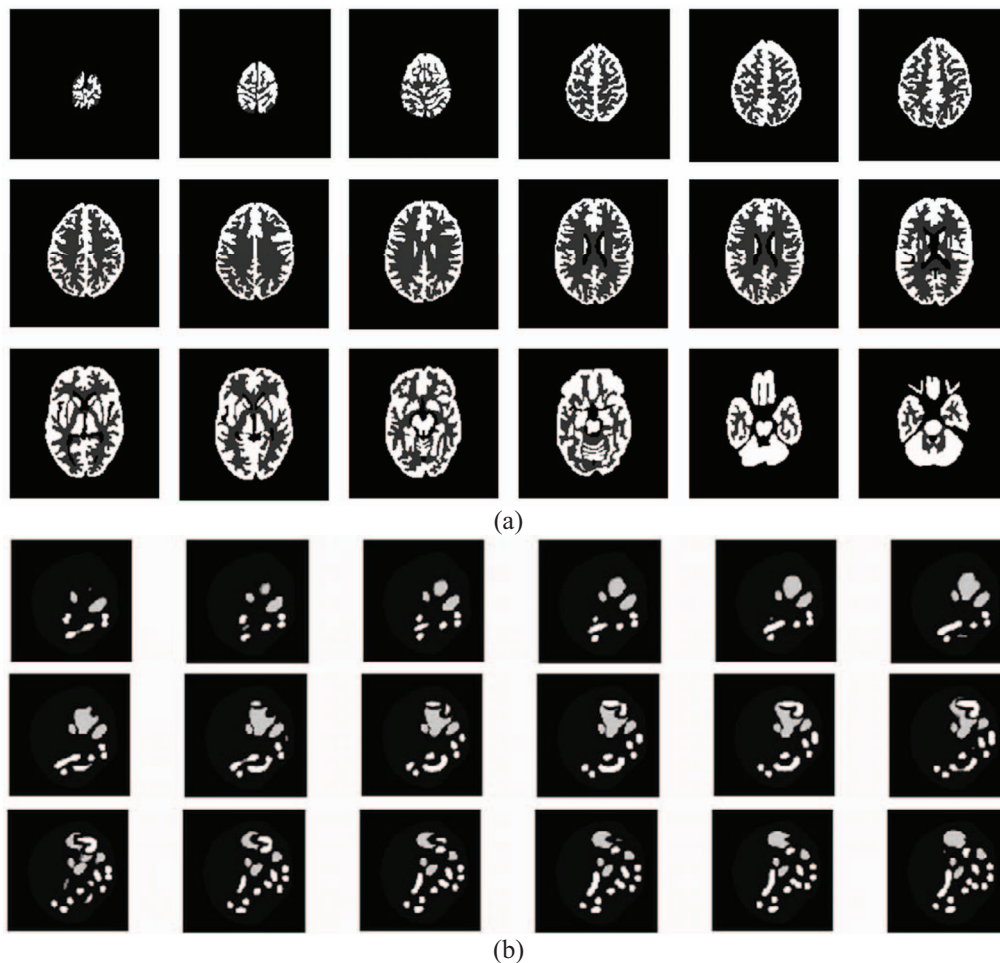


Fig.1. The digital phantoms used for the development of the method: a) the Hoffman brain phantom and b) some slices (n° 23 to n° 40) from MOBY phantom.

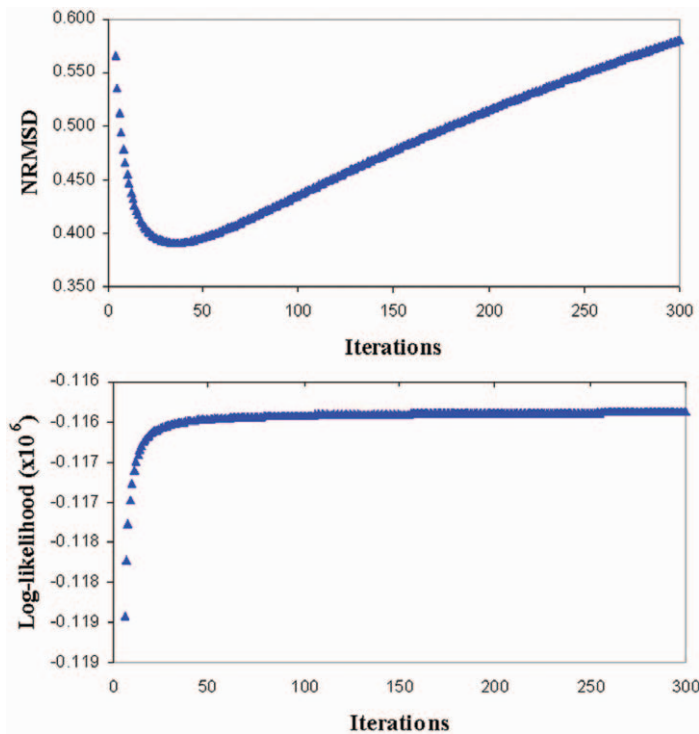


Fig. 2 The NRMSD and log-likelihood curves for the Hoffman brain phantom slice n° 14 for 200,000 measured counts

III. RESULTS

Fig. 2 shows the evolution of the normalized root mean square deviation (NRMSD) [9] and the log-likelihood curve, for the reconstructed images from slice n° 14 of the Hoffman brain phantom (200,000 counts), starting from a uniform image as initial guess. Some examples of the reconstructed images are illustrated in Fig. 3. From this figure it can be observed that there is an improvement of the reconstructed image quality during the first iterations (2nd iteration shown) to the iteration where minimum NRMSD occurs (30th iteration) and after that, the image progressively deteriorates as further noise is added. This effect is also represented in the NRMSD curve in Fig. 2, whereas the log-likelihood curves monotonically increases, as expected from the application of the MLEM algorithm.

From equation (2) it is clear that the evolution of the values of the PUC reflects the convergence rate for a particular image. Motivated by this assumption we have studied further the statistical behavior of the PUC for all non-zero pixels of the reconstructed image versus the number of iterations. Fig. 4 shows the histograms of the PUC values for the Hoffman brain phantom slice n° 14 at the 10th, 50th and 110th MLEM iteration. It can be observed that these histograms have two components:

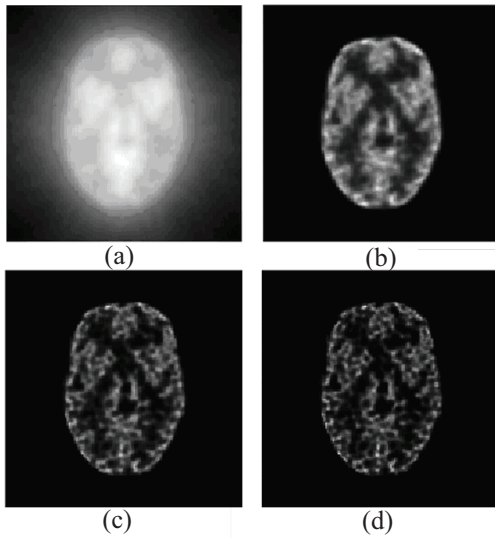


Fig. 3. Hoffman brain phantom slice n° 14, with 200,000 counts acquired, reconstructed after: a) 2, b) 30, c) 110 and d) 210 iterations.

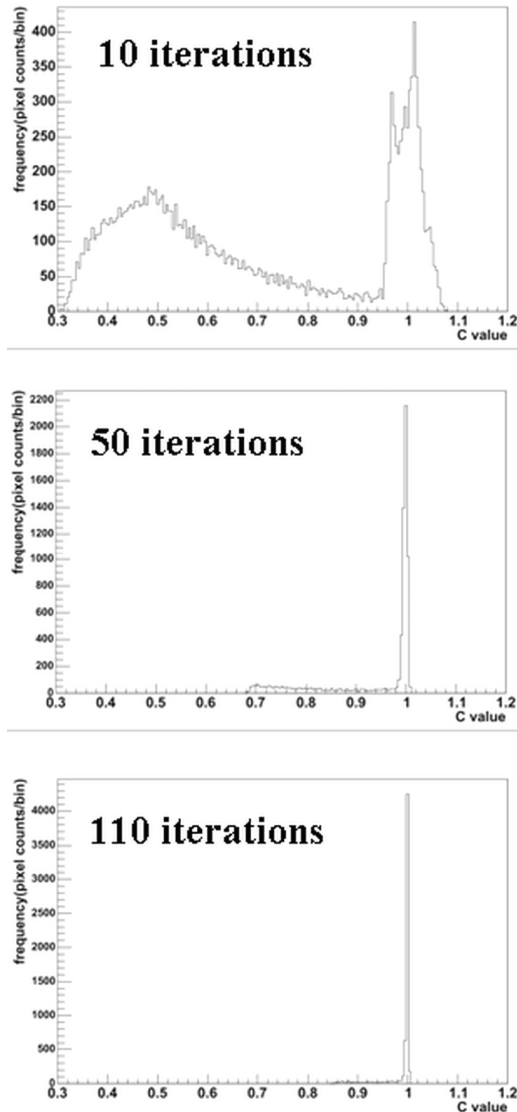


Fig. 4. Histograms show the distribution of the values of the updating coefficients C . As the iteration process progresses, the PUC values shift around 1.0.

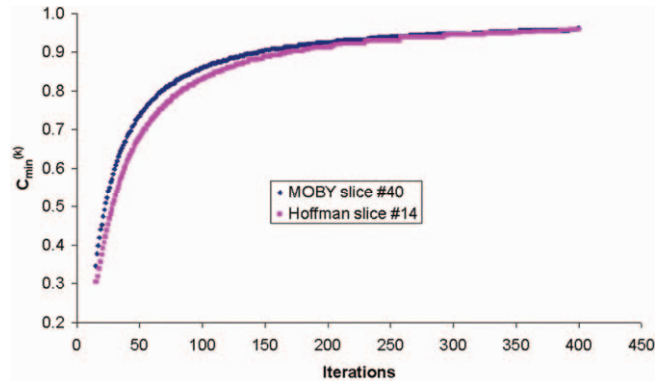


Fig. 5 $C_{\min}^{(k)}$ versus number of iterations for MOBY phantom slice n° 40 and Hoffman slice n° 14.

- (a) a concentration of values around 1.0, which correspond to the PUC of those pixels for which the true phantom value has been closely approximated and
- (b) a region with values lower than 1.0 (tail) which corresponds to the PUC values of those pixels that have not yet reached their true values at that particular point of the iterative process.

This effect is expected, given the non-uniform convergence rate of the MLEM algorithm for the different image regions. Therefore, it can be concluded that for a pixel i that lies in the non-zero activity areas of the true image:

$$\lim_{k \rightarrow \infty} C(i) = 1.0 \quad (6)$$

The tail region in the histograms shown in Fig. 4, corresponds to the part of the image that has not been fully reconstructed. Hence, it can be considered that the lower values (most left ones) in these histograms, and particularly the minimum value of the tail, correspond to the pixel values that contribute mostly to the noise level in the reconstructed image. We define a variable:

$$C_{\min}^{(k)} = \min\{C^{(k)}(i), i = 1, 2, \dots, I\} \quad (7)$$

where I is the total number of pixels with non-zero activity in the image and k is the iteration number. $C_{\min}^{(k)}$ is the minimum value of the vector of the PUC among the non-zero pixels of the reconstructed image at the iteration k . $C_{\min}^{(k)}$ can be easily calculated from each histogram.

We studied further the relationship between the log-likelihood and the minimum value of the PUC, as well as the dependence of this variable on the iteration number and the number of measured counts. For that purpose we considered the images from the Hoffman brain and MOBY phantoms as the true activity distributions and we simulated the data generation and detection process as described in section II.D. The log-likelihood for each image and its corresponding sinogram were calculated and as a result of the MLEM-based image reconstruction has been considered the image for which equation (5) has been firstly achieved.

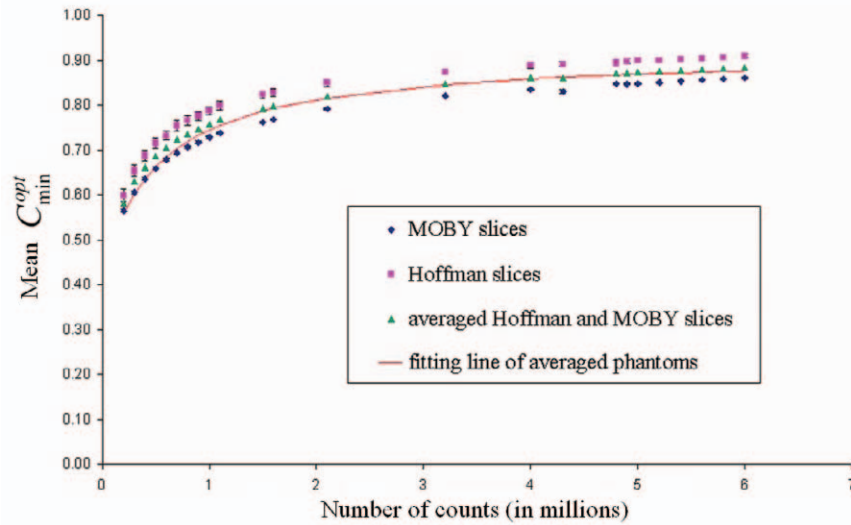


Fig. 6. Mean C_{\min}^{opt} values versus number of counts for Hoffman and MOBY slices, the averaged slices and the fitting line of averaged slices.

Fig. 5 shows an example of the evolution of the $C_{\min}^{(k)}$ value for an experiment with the Hoffman slice n° 14 for 2.1 million counts, and another with the MOBY slice n° 40 for 90,000 counts in the source. The figure shows that $C_{\min}^{(k)}$ increases monotonically with the iteration numbers.

As a next step, we simulated the Hoffman and MOBY phantoms with a range from 0.2 million to 6.0 million counts. Each image has been reconstructed using image grid 128×128 pixels. C_{\min}^k values were calculated for each activity level, averaged over all slices. For each image slice we recorded the new quantity C_{\min}^{opt} namely the minimum value C_{\min}^n of the PUC for the image obtained at the iteration $k = n$ at which the criterion of equation (5) is achieved for the first time. Fig. 6 shows the average C_{\min}^{opt} values as a function of the activity distribution for all slices of the Hoffman and MOBY phantoms. This figure shows that the mean C_{\min}^{opt} values increase monotonically as a function of the activity distribution levels, with similar shapes for both curves. From Fig. 6 it can be observed that the mean C_{\min}^{opt} depends on the number of measured counts. Furthermore there is a characteristic clustering of the C_{\min}^{opt} values for a given count number implying a little dependence on the shape of the imaged object.

Moreover, Fig. 6 shows the curve that results from the averaging of the two individual curves from the two experiments described before. Using that average curve one can estimate the C_{\min}^{opt} for a given number of counts, independently of the shape of the activity distribution in the source. Since in real PET scans the number of detected counts is known, the discovery of a relationship between C_{\min}^{opt} and the detected number of counts would in fact establish a

relationship between the log-likelihood inherent in the acquired data and the true image from the one part and the iteration at which this log-likelihood value is reached (approximately) during the image reconstruction process.

In order to parameterize quantitatively the dependence of C_{\min}^{opt} on the number of counts, we fitted the averaged curve shown in Fig. 6. A fitting method has been applied using the weighted average and associated errors of mean C_{\min}^{opt} . Different fitting models have been tested such as linear, polynomial or Gaussian equations. In Table I the R^2 values produced by various equations are shown. Each of these values gives information about the goodness of fit of the equation. An R^2 of 1.0 indicates that the selected model perfectly fits the data.

TABLE I
 R^2 VALUES FOR DIFFERENT FITTING EQUATIONS

Equation	R^2 value
Rational	0.9986
4 th degree polynomial	0.9927
6 th degree polynomial	0.990
Cubic polynomial	0.9796
Gaussian	0.9161
Quadratic	0.9302

The most accurate, according both to visual inspection and by producing the best R^2 value as shown in Table I, resulted the following rational form:

$$K = A \frac{N + \alpha}{N + b} \quad (8)$$

where N is the number of counts in the image, expressed in millions. The behavior of mean C_{\min}^{opt} can be expressed as a function of the number of counts N , a parameter known in all cases, including real PET scans.

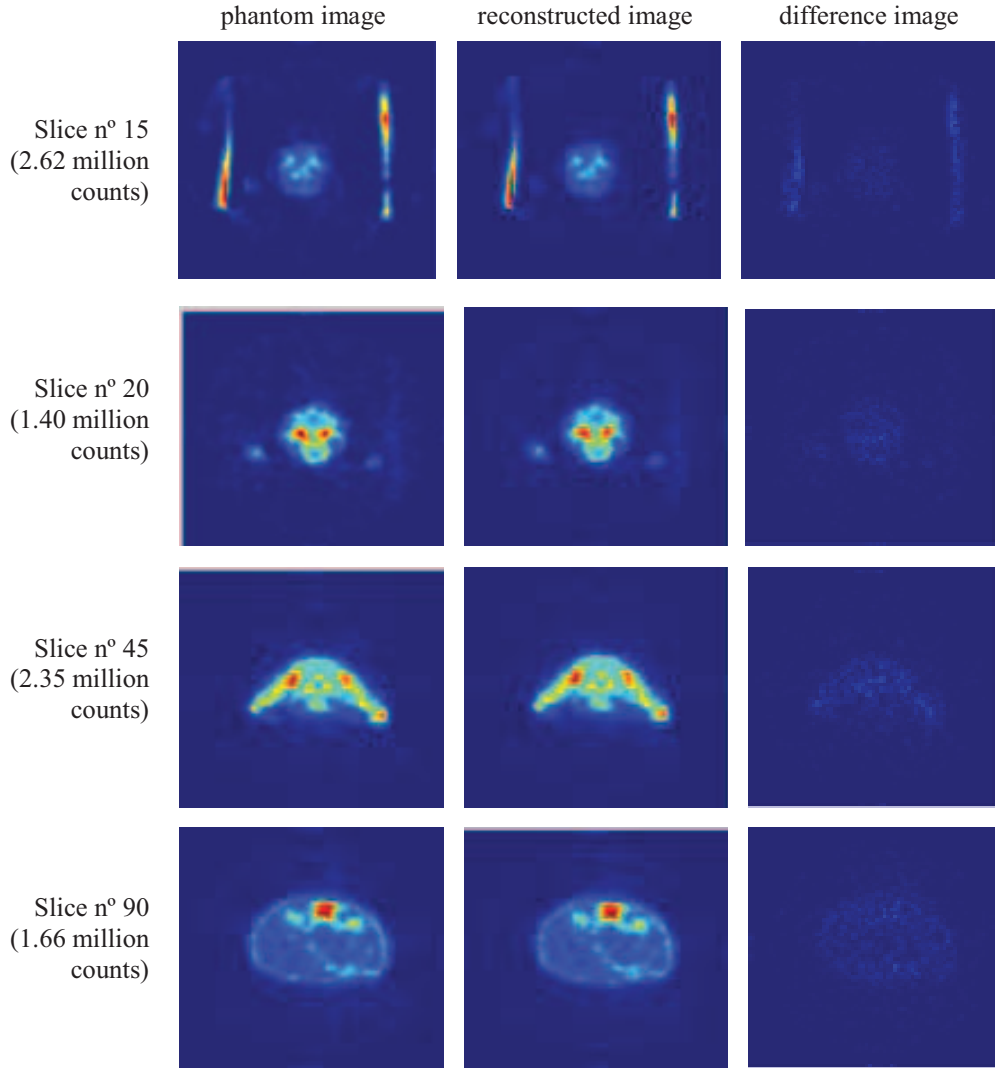


Fig. 7. The validation of stopping rule using the Digimouse slices n° 15, 20, 45 and 90. The images shown are the phantom slices, the reconstructed images and the difference between them

The parameters A , a and b have been specified using the fitting tool of MATLAB as follows:

$$\begin{aligned} A &= 0.9169 \pm 4.3e-03 \\ \alpha &= 0.2756 \pm 34e-03 \\ b &= 0.5413 \pm 53e-03 \end{aligned} \quad (9)$$

TABLE II

DETAILS ABOUT THE RECONSTRUCTION USING STOPPING RULE			
	$N (\times 10^6)$	K^*	n (stopping iteration n^o)
Slice #15	2.62	0.8330	95
Slice #20	1.40	0.7807	87
Slice #45	2.35	0.8254	87
Slice #90	1.66	0.7970	71

*calculated from eq. (8)

IV. DISCUSSION

Based on the current results, the value of K , as it can be calculated from equation (8), can provide an indicator for the

instance of the iterative process at which the reconstructed image reaches a level of log-likelihood that would satisfy equation (5), and therefore constitutes the most appropriate result of this iterative image reconstruction process. The MLEM algorithm can therefore be stopped at the iteration n where :

$$C_{\min}^{(n)} \geq K \quad (10)$$

In other words we suggest that one can consider terminating the MLEM iterations at the iteration n at which the minimum value of the pixel updating coefficients

For the validation of the proposed methodology a different set of phantom images have been used. This set of real scanned images originated from the Digimouse phantom [12]. Using Digimouse slices as input, the projection data were generated with the Monte Carlo methods described in section II.D, with a determined number of counts for each image slice. Using equation (8) the corresponding K values were estimated. The MLEM algorithm was stopped when the condition described in equation (10) was met.

For the Digimouse slices n° 15, 20, 45 and 90, with n° of counts 2.62, 1.40, 2.35 and 1.66 million respectively, the MLEM reconstructed was stopped at iteration number 95, 87, 87 and 71 respectively. These data are also summarized in Table II. Fig. 7 shows the phantom image on which the generation of the detected counts was based, and the corresponding reconstructed image as well as the difference between the original phantom image and the reconstructed one are shown for each one of the four Digimouse slices selected. The difference images between the phantom and reconstructed show that the images produced using the proposed stopping rule are very similar to original phantom images, demonstrating the goodness of the methodology developed here.

Fig. 8 shows some line profiles taken from the phantom and the reconstructed images for the four exemplary Digimouse images shown in Fig. 8. There is a very close match between each pair of line profiles, something that re-enforces the accuracy of the methodology developed.

V. CONCLUSIONS

We have developed a methodology for the monitoring of the image quality, in terms of the noise characteristics, of the images reconstructed using the MLEM algorithm on synthetic PET data, produced by Monte Carlo techniques. This methodology is based on the hypothesis that a good criterion to stop the MLEM-based iterative process could be that the reconstructed image, taking into account the acquired data in each line of response, produces a log-likelihood value approximately near the log-likelihood value of the true image.

The methodology developed here, based on the properties of the pixel updating coefficients in the MLEM-based image reconstruction has been shown to produce images very close to the phantom images, in the case of simulation studies. At a second step, the method has been validated using an independent simulation study, in which the original activity distribution in the source has been considered unknown, when selecting the stopping point of the iterative process. The proposed criterion depends on the projection data and the PET camera geometry, for which the parameters A , a and b of equation (8) need to be calculated. Further work is needed in order to establish the dependence of these parameters on PET scanner geometry. Work is on-going in order to determine how the developed methodology is affected by the various noise effects in PET scans, such as attenuation, randoms, scattering, etc. This work is currently being carried out with realistic data produced by simulations using the GATE platform.

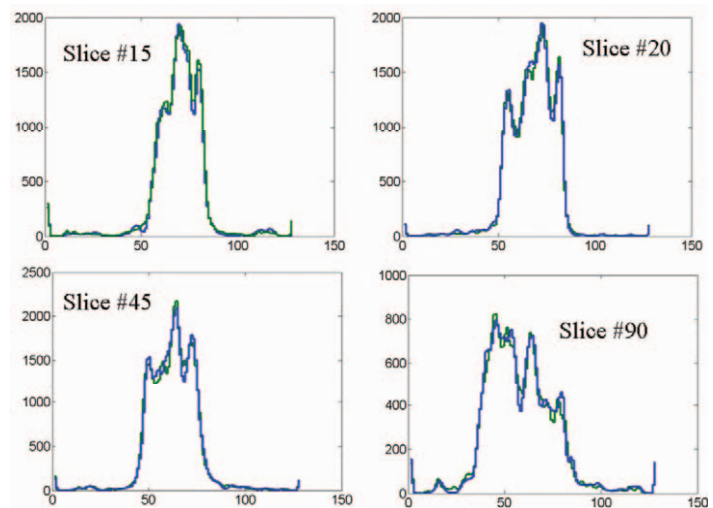


Fig. 8. Line profiles from the phantom (blue lines) and reconstructed (green lines) images taken from the Digimouse slices shown in Fig. 7.

REFERENCES

- [1] L.A. Shepp, Y.Vardi, "Maximum Likelihood Reconstruction for Emission Tomography," *IEEE Trans. Med. Imag.*, Vol. 1, n° 2: 113-121, 1982.
- [2] M. Hudson, R. S. Larkin, "Accelerated Image Reconstruction using Ordered Subsets of Projection Data," *IEEE Trans. Med. Imag.* 13: 601-609, 1994
- [3] D. W. Townsend, "Physical Principles and Technology of Clinical PET Imaging," *Ann Acad Med Singapore*, 33(2): 133-145, 2004.
- [4] D. J. Kadmas, "Statistically Regularized and Adaptive EM Reconstruction for Emission Computed Tomography", *IEEE Trans. Nucl. Sci.*, Vol. 48, N° 3, pp. 790-798, June 2001.
- [5] E. Veklerov, J. Llacer, "Stopping Rule for the MLE Algorithm Based on Statistical Hypothesis Testing", *IEEE Trans. Med. Imag.*, Vol MI-6, No 4, 1987.
- [6] N. Bissantz, B. A. Mair and A. Munk, "A multi-scale stopping criterion for MLEM reconstructions in PET", *IEEE Medical Imaging Conference*, San Diego, USA. October 29 – November 4, 2006.
- [7] G. Kontaxakis, G. Tzanakos, "A stopping criterion for the iterative EM-MLE image reconstruction for PET," *SPIE, Medical Imaging 1996: Image Processing*, M. H. Loew, K.M. Hanson, Eds., vol. 2710: 133-144, 1996.
- [8] A. Gaitanis, G. Kontaxakis, G. Panayiotakis, G. Spyrou, G. Tzanakos, "The role of the updating coefficient of the ML-EM algorithm in PET image reconstruction," *Eur. J. Nucl. Med Mol. Imag.*, 33 (Suppl. 2):314, 2006.
- [9] A. Gaitanis, G. Kontaxakis, G. Spyrou, G. Panayiotakis, G. Tzanakos, "PET image reconstruction: A stopping rule for the MLEM algorithm based on properties of the updating coefficients", *Comp. Med. Imag. Graph.*, 2009 doi:10.1016/j.compmedimag.2009.07.006.
- [10] W.P. Segars, B.M.W. Tsui, E.C. Frey, G.A. Johnson, and S.S. Berr, "Development of a 4D digital mouse phantom for molecular imaging research". *Mol. Imag. Biol.*, Vol. 6, Issue 3, pp. 149-159, 2004
- [11] E. J. Hoffman, P. D. Cutler, W. M. Digby, J. C. Mazziotta, "3D phantom to simulate cerebral blood flow and metabolic images for PET," *IEEE Trans. Nucl. Sci.*, NS-37(2): 616-620, 1990.
- [12] B. Dodgas, D. Stout, A. F. Chatziioannou and R. M. Leahy, "Digimouse: a 3D whole body mouse atlas from CT and cryosection data", *Phys. Med. Biol.* 52, pp. 577-587, 2007.